Cell morphogenesis via self-propelled treadmilling actin waves

Kio Yagami[1], Kentarou Baba[1], Takunori Minegishi[1], Shinji Misu[1], Hiroko Katsuno-Kambe[1], Kazunori Okano[2], Yuichi Sakumura[3], Yoichiroh Hosokawa[2] and Naoyuki Inagaki[1,4,*]

[1]Laboratory of Systems Neurobiology and Medicine, Division of Biological Science, Nara Institute of Science and Technology, Ikoma, Nara 630-0192, Japan.

[2]Bio-Process Engineering Laboratory, Division of Materials Science, Nara Institute of Science and Technology, Ikoma, Nara 630-0192, Japan.

[3]Laboratory of Data-driven Biology, Division of Biological Science, Nara Institute of Science and Technology, Ikoma, Nara 630-0192, Japan.

[4]Lead Contact

*Correspondence: ninagaki@bs.naist.jp

SUMMARY

Actin dynamics mediate cell morphogenesis. Actin filaments polymerize outward at cell protrusions such as the leading edge of migrating cells, thereby pushing the membrane to protrude. The current paradigm explains that actin dynamics are regulated by cell signaling. However, it is unclear how cells spontaneously form actin-based protrusions even without a specific local signaling cue. We found that arrays of treadmilling actin filaments emerge widely in migrating cells and move in the direction of polymerization as actin waves. Their arrival at the cell periphery pushes the plasma membrane to protrude. Furthermore, they accumulate at protrusions without local signaling cues, similar to self-propelled particles colliding with a boundary. This leads to further growth of protrusions, thereby promoting spontaneous formation of the leading edge for migration. We propose that the self-propelled actin waves drive robust formation of protrusions for cell morphogenesis, through their abilities to self-accumulate into protrusions and push the membrane.

KEYWORDS: Cell protrusion, Cell morphogenesis, Lamellipodium, Filopodium, Cell migration, Actin treadmilling, Actin wave, Self-propelled Brownian particle, Active particle, Microswimmer

INTRODUCTION

Spatial regulation of actin dynamics is crucial for controlling cell shape and motility[1-4]. Arrays of dynamic actin filaments are located in various cell protrusions, such as the lamellipodia and filopodia of migrating cells[1,3-5], neurite tips and dendritic spines in neurons[6-8], microvilli and cell-cell adhesion sites in epithelial cells[9-12], hair cell stereocilia[13], invadopodia[14,15], and phagocytosis cups[16]. In these regions, actin filaments polymerize outward and push the membrane to protrude. The filament arrays often undergo proximal disassembly which results in treadmilling[1-4,17]. In this process, actin monomers bound to ATP assemble at the plus ends of actin filaments, followed by ATP hydrolysis within the filaments. The filaments disassemble from the minus ends because ADP-bound actin molecules destabilize them. ADP in the subunit is replaced with ATP, enabling its reuse in polymerization. Thus, actin filaments undergo directional polymerization and disassembly using the energy derived from ATP hydrolysis[1-4,17]. The prevailing view is that actin filament nucleators and elongators, such as the Arp2/3 complex, formins, FMNL and Ena/VASP, control local actin assembly under Rho GTPase signaling[1,3,4]. On the other hand, actin disassembly-promoting proteins, such as ADF/cofilin, regulate actin turnover[2,17,18]. However, it remains unclear how actin filaments can self-assemble to form protrusions, even without apparent local signaling.

Dynamic actin filaments undergo wave-like propagations in various cell types[19-22]. Many of these propagations have been explained by the reaction-diffusion mechanism[20-23]. On the other hand, we previously reported that actin treadmilling propels the translocation of actin waves and actin-binding proteins towards the axonal tips of neurons in culture and tissue[24]. In this study, we identified actin waves that translocate via treadmilling instead of the reaction-diffusion mechanism in non-neuronal cells. The arrival of actin waves at the cell periphery results in the formation of protrusions. Notably, the actin waves spontaneously accumulate at cell protrusions in a manner similar to self-propelled particles (also known as self-propelled Brownian particles, active particles or microswimmers)[25]. The self-propelled particles are substances that undergo active and random motion; they have been extensively investigated in the fields of physics[25-27] and soft matter[28]. This self-propelled motion mediates the accumulation of outward-polymerizing actin filaments at the cell periphery and protrusive regions even without

local signaling. Inhibition of actin wave translocation disrupts spontaneous formation of the leading edge for migration.

RESULTS

Actin waves emerge widely in cells and move in random directions

To investigate the mechanism underlying the spatial regulation of actin dynamics, we analyzed a subline of glioma U251 cells that actively form lamellipodia and filopodia (Figure S1A). These cells spontaneously polarize and migrate in the absence of growth factor stimulation (Figure S1B)[29]. Actin dynamics were visualized by total internal reflection fluorescence (TIRF) microscopy using the actin filament marker LifeAct. In addition to prominent actin filaments at the leading edge (asterisk, Figure 1A), arrays of actin filaments that form filopodium-like and lamellipodium-like structures emerged widely in the cytoplasm, moved in random directions, and disappeared (Video S1). The majority of them were filopodium-like (arrowheads, Figure 1B and Video S1 right); some emerged and separated (yellow and cyan arrowheads) from lamellipodium-like structures (arrows) or branched off (green arrowheads) from filopodium-like structures. We also observed lamellipodium-like structures expanded from the filopodium-like structures (arrows, Figure S1C, Video S1 right), indicating their interchangeability. Notably, the filopodium-like structures changed the direction of their translocation randomly (yellow arrowheads, Figure 1B and Video S1 right). Similar actin waves were also observed in COS7 cells (Figure S1D, Video S1), suggesting that they are not cell type-specific. Herein, we analyzed the filopodium-like and lamellipodium-like structures that move within the cells as filopodium-type and lamellipodium-type actin waves, respectively.

3D imaging with confocal deconvolution microscopy revealed actin waves moving along the dorsal plasma membrane (Figure 1C) as well as waves translocating through the cytoplasm without interacting with the plasma membrane (Figure 1D, Video S2). In addition, a combination of TIRF microscopy, which visualizes the region near the ventral plasma membrane, and epifluorescence microscopy, which visualizes the entire cell thickness, revealed a substantial fraction of waves translocating along the ventral plasma membrane (arrowheads, Figure 1E, Video S2), as well as waves travelling apart from the adhesive substrate at the leading edge (arrowheads, Figure 1F, Video S2).

Actin waves translocate by treadmilling

Next, we examined the actin dynamics within waves by labelling actin filaments with EGFP-LifeAct, and monitoring actin molecules in the filaments by speckle imaging of HaloTag-actin[30]. During the forward translocation of filopodium-type and lamellipodium-type waves along the ventral membrane (green lines, Figures 2A and S1E) individual actin molecules moved retrogradely within the filaments (magenta lines, Video S3). Similar retrograde movements of actin molecules were observed in filopodium-type waves with no interaction with the plasma membrane (Figure S1F), indicating that actin waves undergo treadmilling and translocate in the direction of polymerization.

We previously reported actin waves that translocate along neuronal axons through treadmilling[24]: their front and rear ends undergo polymerization and disassembly, respectively (black arrows, Figure 2B left)[21,24]. In addition, actin filaments in waves are weakly anchored to the plasma membrane and adhesive substrate, through the linker molecules shootin1a and cortactin as well as the cell adhesion molecule L1[24,31]. This anchoring impedes the retrograde flow (slippage) of treadmilling actin filaments (magenta arrow, Figure 2B). Thus, the actin polymerization/disassembly rate exceeds the retrograde flow rate, which results in the forward translocation of the front and rear ends of waves (green arrow). During the translocation, local concentrations of actin subunits and actin-binding proteins decrease at the front by polymerization and increase at the rear by disassembly, resulting in their diffusion along the local concentration gradients (black arrows, Figure 2B). Accompanied by this directional diffusion, actin waves translocate actin and actin-binding proteins along axons[24,32].

Immunoblot analyses showed that U251 cells express, shootin1b, cortactin and L1 (Figure S1G); shootin1b is a splicing variant of shootin1a that also mediates the actin-L1 linkage[33]. Shootin1b co-localized with actin filaments in waves (arrowheads, Figure 2C). Inhibition of actin polymerization in waves by cytochalasin B at a low concentration (0.05 μM)[24] decreased the velocity of actin wave translocation (Figure S1H). The Arp2/3 complex inhibitor CK666 (100 μM)[34] or a relatively non-specific formin inhibitor SMIFH2 (5 μM)[35] also reduced the velocity of actin wave (Figure 2D), indicating that wave translocation is propelled by actin assembly. Furthermore, shootin1b knockout (KO) (Figure S1I) resulted in an increase in the retrograde flow velocity of actin filaments in waves, without affecting the polymerization rate (Figure 2E), indicating that shootin1b

anchors treadmilling actin filaments to the plasma membrane and adhesive substrate (for explanation see also Figure S1J). This in turn reduced the velocity of actin wave translocation (Figure 2E). Together, these results indicate that actin waves in U251 cells translocate via actin treadmilling and that shootin1b promotes their translocation by impeding the retrograde flow (Figure 2B left).

We have also observed actin waves moving apart from the adhesive substrate (Figures 1C and 1F), as well as in the cytoplasm without interacting with the plasma membrane (Figure 1D). Moreover, the inhibition of actin filament anchorage to the plasma membrane by shootin1b KO did not completely prevent wave translocation (Figure 2E). The cytoplasm represents a viscous and crowded intracellular environment that contains proteins, macromolecules, and cytoskeletal components[36,37]. Actin waves may also move via treadmilling without anchoring to the membrane and adhesive substrate when retrograde actin filament flow is mechanically obstructed in the intracellular environments (Figure 2B right).

Actin waves as precursors of protrusions

When filopodium-type waves arrived at the cell periphery without protrusions, they pushed the plasma membrane to form filopodia (arrowheads, Figure 3A, Video S4). The arrival of lamellipodium-type waves at the membrane also resulted in the formation of lamellipodia (yellow arrows, Figure 3B, Video S5), as reported[38,39]. In addition, we also observed filopodium-type waves entering into pre-existing lamellipodia (arrowheads, Figure 3C, Video S6 left) and filopodia (Video S6 right). Their entrance in the lamellipodia resulted in local actin filament accumulation and lamellipodial expansion (arrows, Figure 3C, Video S6 left). Some filopodia and lamellipodia derived from actin waves continued to move laterally along the membrane (Figures 3A and 3B), consistent with previous reports that filopodia and lamellipodia move dynamically along the lateral side of neuronal[32,40] and non-neuronal[41,42] cells. We also noted lamellipodium-type waves (yellow arrows, Figure 3B, Video S5) that merged with the pre-existing lamellipodia (cyan arrows) through their lateral movement.

If the lateral movements of filopodia and lamellipodia are driven by the mechanism of wave translocation, their velocity would be related to the angle θ of the polymerizing actin filaments with respect to the membrane (Figure 3D). To examine this

possibility, we focused on the motion of filopodium-type waves because the majority of waves are the filopodium-type and filopodium- and lamellipodium-types are interchangeable (Video S1). In addition, it was difficult to monitor the direction of actin filaments in lamellipodium-type waves (Figures 1B and 3B). Time-lapse measurements of both the angle θ and the velocity of the filopodial lateral movement (V_L) (Figure 3E, Video S7) demonstrated that the velocity closely matched the cosine θ for the average velocity of the ventrally translocating filopodium-type waves before arriving at the membrane (V_V) (2.0 ± 0.2 μm/min, Figures 2D and 3E), indicating agreement between the data and the prediction based on the mechanism. Together, these data suggest that treadmilling actin waves and filopodia/lamellipodia are equivalent structures and that actin waves serve as precursors of filopodia and lamellipodia. Therefore, the filopodia and lamellipodia that move laterally along the membrane are also termed actin waves in this study.

Actin filaments spontaneously accumulate at protrusions

We observed translocation of filopodium-type and lamellipodium-type actin waves in protrusive regions through their lateral movement (Figures 4A and 4B, Video S8), suggesting that actin dynamics are affected by cell shape. In addition, a previous study reported that different cell types confined to square adhesive islands preferentially extend filopodia and lamellipodia from their corners[41]. To determine the potential influence of cell shape on actin dynamics, we prepared a triangular pattern of adhesive laminin on the substrate (Figure 4C). U251 cells showed the triangular shape when cultured on the laminin-coated adhesive island (Figure 4D). While actin filaments were preferentially localized at the leading edge of unconstrained cells, they accumulated at the corners of triangular cells (Figure 4D). Live imaging of U251 cells labelled with LifeAct-mCherry revealed the dynamic accumulation of actin filaments at the corners (Figure 4E and Video S9). Actin waves travelled along the lateral edge, resulting in local accumulation of actin filaments at the corners upon arrival (arrowheads). Surprisingly, in contrast to the current view that the Arp2/3 complex promotes membrane protrusion by activating actin polymerization, a component of the Arp2/3 complex, ARPC2, accumulated together with actin filaments at the protruding corners in the absence of local growth factor stimulation

(Figure 4D).

Actin waves mediate actin filament accumulation at cell periphery and protrusions

Since the arrival of actin waves increased actin filaments at the protrusive areas (arrowheads, Figure 4E), we hypothesized that they mediate the accumulation of actin filaments at cell protrusions. To examine this possibility, we constructed a mathematical model to describe filopodium-type waves, as we could observe actin filaments clearly in these waves (Figure 1B). Our model consists of the following properties of actin wave dynamics (see STAR METHODS for details).

1. Actin waves emerge at random locations within the cell and move in random directions (Video S1).
2. Actin waves frequently change their direction of translocation and disappear at the end of their lifetime (Video S1).
3. Actin waves re-emerge at the location where the preceding waves disappear (see STAR METHODS).
4. Actin waves located at the cell periphery move laterally along the cell membrane. The velocity of the lateral movement conforms to the $\cos\theta$ of the mean velocity of ventrally translocating waves (V_V), where θ is the angle of the direction of actin filaments relative to the cell membrane (Figure 3E).

All the model parameters, i.e., lifetime, length, moving velocity and degree of the change in moving direction, were obtained from our quantitative experimental data (Figures S2A-S2E). The actin waves described by the model accumulated dynamically at the corners of the triangular cells (Figure 5A and Video S10), as observed in U251 cells. Using this mathematical model, we further analyzed the movement of actin waves in cells with different corner angles (i.e., 30°, 60°, 120° or 180°; Figure S2F) and quantified the relative accumulation of actin filaments at the cell periphery and corners (Figure S2G). The actin waves accumulated at the cell periphery (Figure S2H). Furthermore, the accumulation of actin waves at the corner increased as the corner angle decreased from 180° to 30° (Figure 5B). To validate this model, we cultured U251 cells using the same

patterns. As predicted, actin filaments accumulated at the periphery (Figure S2I) and corners of the cells in a corner angle-dependent manner (Figure 5C).

We further examined the effect of inhibiting the actin wave via knocking out shootin1b. Interestingly, shootin1b KO not only reduced the translocation velocity (Figure 2E) but also the lifetime (Figures S2A-S2C) of actin waves. Introduction of these parameters (i.e., wave velocity and lifetime derived from shootin1b KO cells) into the model disrupted actin accumulation at the cell periphery and corners (Figure 5D and Video S10). Consistently, shootin1b KO inhibited actin accumulation at the cell periphery and corners of U251 cells (Figure 5E). Together, these data indicate that treadmilling actin waves mediate actin filament accumulation at cell periphery and protrusions.

Actin waves drive spontaneous formation of the leading edge for cell migration

Next, the role of actin waves in cell morphogenesis was analyzed using U251cells with the deformable plasma membrane. Wild-type (WT) cells typically exhibited a polarized morphology with a large lamellipodium (Figure 6A). On the other hand, inhibition of actin waves by shootin1b KO resulted in the fragmentation of lamellipodia (Figure 6A), leading to a decrease in the lamellipodial coverage rate at the cell periphery (Figure 6B). Accordingly, the unilateral integration of lamellipodium was disrupted, resulting in a decrease in the degree of cell polarity (Figure 6C). Shootin1b depletion also reduced filopodial length (Figure S3B).

To analyze how actin waves drive cell polarization, we monitored the recovery of cell polarity after latrunculin A-induced actin filament disassembly[43]. Treatment of WT U251 cells with 100 nM latrunculin A disrupted their polarized morphology (Figure 6D and Video S11). During recovery following latrunculin A washout, the cells formed multiple foci of small lamellipodia enriched with actin filaments (asterisks, Figure 6D). The foci then grew and moved laterally (cyan arrows) or expanded laterally (yellow arrows), integrating into a large lamellipodium. Through these processes, the cells eventually formed the leading edge and acquired polarity.

We further monitored the motion of actin waves in a two-dimensional (2D) model of cells bearing protrusions that mimic the nascent and integrated lamellipodia. As shown in Figure 6E, actin waves in the model highly accumulated in the nascent lamellipodia. In addition, although our model does not include the thinner thickness of

the leading edge in the 3D condition, actin waves accumulated moderately in the integrated lamellipodium located at the convex leading edge (Figure 6F). Introduction of the parameters derived from shootin1b KO cells (Figures 2E and S2A-S2C) into the model inhibited actin wave accumulation at the nascent and integrated lamellipodia (Figures 6E and 6F).

Consistently with the modeling data, shootin1b deletion in glioma cells inhibited the lateral movement, expansion, and integration of nascent lamellipodium (asterisks, Figure 6G and Video S11). This in turn delayed the onset of cell migration after recovery from the latrunculin A treatment (Figure S3E). As previously reported, shootin1b also mediates the generation of traction force at the leading edge through its interaction with treadmilling actin filaments[33]. Therefore, the impairment of lamellipodial integration resulting from shootin1b KO can be attributed to the combined effects of reduced accumulation of treadmilling actin filaments at lamellipodia (Figures 6E and 6F) and diminished force generation there. Taken together, we conclude that treadmilling actin waves of glioma cells drive spontaneous formation of the leading edge by expanding the nascent lamellipodia.

DISCUSSION

Self-propelled motion of treadmilling actin waves

Treadmilling is an inherent property of actin dynamics. We demonstrate that arrays of treadmilling actin filaments emerge widely in cells, move as actin waves, and disappear. During the translocation, the front and rear ends of waves move forward via polymerization and disassembly, respectively (blue arrows, Figure 7A). Shootin1b facilitates the wave translocation by anchoring treadmilling actin filaments to the plasma membrane and extracellular environments, and impeding their retrograde flow (Figure 2B left). As the local concentrations of actin subunits and actin-binding proteins decrease at the front by polymerization and increase at the rear by disassembly, they are thought to diffuse along the local concentration gradients (red and green arrows, Figure 7A). Thus, accompanied by the directional diffusion, treadmilling actin waves mediate the translocation of actin and actin-binding proteins.

Most of actin wave propagations in cells have been explained by the reaction-diffusion mechanism that involves positive and negative feedback interactions between

excitable and inhibitory components[20-23]. On the other hand, actin waves observed here randomly change the direction of movement in a manner similar to self-propelled particles[25,26,28]. Their trapping in protrusive regions (Figures 5B and 5C) also resembles the motion of the self-propelled particles colliding with a boundary[26]. These analogies support our conclusion that the treadmilling actin waves move by self-propelling rather than via the reaction-diffusion mechanism, although we do not rule out waves that travel via other mechanisms, Treadmilling actin waves are not stable particles: actin subunits are continuously exchanged between waves and the cytoplasm during translocation (Figure 7A). In addition, our proposed mechanism explains the translocation of treadmilling actin waves, but it does not address the question of how they emerge and disappear.

Actin waves self-accumulate into cell protrusions for polarization

The present study demonstrated that actin filaments localize not only at the region where they polymerize but also where actin waves arrive. The arrival of actin waves at the cell periphery mediates the accumulation of outward-polymerizing actin filaments, thereby pushing the membrane to protrude (gray arrows, Figure 7B). When actin waves encounter the membrane border, they undergo lateral translocation, depending on the direction of actin filaments relative to the membrane (yellow arrows, Figure 7C). This lateral movement traps outward-polymerizing actin filaments and actin binding proteins at protrusive regions (Figure 4D), leading to their further growth (gray arrows, Figure 7C). Here, actin accumulation at protrusions (green arrow, Figure 7D) constitutes a positive feedback interaction with actin-based cell protrusion (red box), thereby conferring robustness to the classical pathway of cellular morphogenesis (black arrows). The self-propelled motion also suppresses the protrusive activities laterally, because wave translocation into the protrusion (yellow arrows, Figure 7C) results in their lateral decrease. Furthermore, the repeated emergence and disappearance of actin waves, in addition to their dynamic motion, contribute to the dynamic movement of protrusions.

In glioma cells, nascent protrusions were integrated into a large leading edge through their lateral movement and expansion (Figure 7E), accompanied by a relative decrease in actin waves at the rear (Figures 6D and 6F, Video S11). These processes would work in concert with other cytoskeletal dynamics, including actomyosin

contraction at the rear[29,44] to polarize cells and initiate cell migration. Membrane tension generated by actin-based protrusions would also support polarization[45,46].

Self-propelled actin waves in cell morphogenesis under extracellular cues

Actin assembly and disassembly are regulated by signaling pathways[1-4,17]. Consequently, the formation, translocation, and disappearance of actin waves are subject to the regulation of extracellular chemical cues and cell signaling (blue arrow, Figure 7D). The inhibition of the Arp2/3 complex or formins reduced the velocity of actin wave translocation (Figure 2D), suggesting that they may act as regulators of actin waves under signaling. Moreover, actin waves may serve as mediators of cellular responses to extracellular topographic cues that deform the plasma membrane from outside (yellow arrow, Figure 7D), as they accumulate at the protrusive and convex regions. This could enable migrating cells to navigate flexibly in three-dimensional environments through mechanical barriers and tissue pores[23,47-49].

Actin filaments undergo outward polymerization not only at the leading edge of migrating cells[1,3,4] but also in various cell protrusions, such as neurite tips and dendritic spines of neurons[6-8], microvilli and cell-cell adhesion sites of epithelial cells[9-12], hair cell stereocilia[13], invadopodia[14,15], and phagocytosis cups[16]. Our modeling data showed that treadmilling actin waves self-accumulate at small protrusive and large convex regions (Figures 6E and 6F), as well as protrusions with different corner angles (Figure 5B). Notably, recent simulation and microswimmer studies have reported that self-propelled particles in vesicles induce various shape deformations and movements similar to those observed in living cells[28,50-52]. Different actin-binding proteins and physical interactions could control the mode of protrusion, either extension or expansion, by altering the shape of the treadmilling filament arrays[3,4,53]. Treadmilling actin waves have the potential to mediate various actin-based cell protrusions due to their ability to self-accumulate into protrusions and push the membrane.

STAR METHODS

Detailed methods are provided in the online version of this paper and include the following:

- **KEY RESOURCES TABLE**
- **RESOURCE AVAILABILITY**
  - Lead Contact
  - Materials Availability
  - Data and Code Availability
- **EXPERIMENTAL MODEL AND SUBJECT DETAILS**
  - Cell culture and transfection
  - Generation of shootin1b KO U251 cells by CRISPR-Cas9
- **METHOD DETAILS**
  - Micropatterning of laminin on the substrate for cell adhesion
  - Immunocytochemistry
  - Immunoblot
  - DNA construction
  - Antibodies
  - TIRF and epifluorescence microscopy
  - Fluorescent speckle imaging of actin wave by TERF microscopy
  - 3D imaging by confocal deconvolution microscopy
  - Mathematical modelling
  - Analyses of actin filament accumulation and lamellipodial formation
  - Analyses of actin filament accumulation and lamellipodial formation
- **QUANTIFICATION AND STATISTICAL ANALYSIS**

SUPPLEMENTAL INFORMATION

Supplemental information can be found online at

ACKNOWLEDGMENTS

We thank Drs. Masatoshi Takeichi (Riken) and Shintaro Suzuki (Kwansei Gakuin Univ) for providing the subline of U251 cells, Dr. Hitoshi Sakano (Fukui Univ) for reading the

manuscript, Drs. Jim Bamburg (CSU), Nir Gov (Weizmann Inst Sci), Carsten Beta (*Potsdam* Univ), Sean Collins (UC Davis), Klemens Rottner (Tech Univ Braunschweig), Giovanni Volpe (Univ *Gothenburg*), Shiro Suetsugu (NAIST), Naoki Watanabe (Kyoto Univ) and Yusuke Maeda (Kyushu Univ) for valuable discussions, and Satoko Shimamura for kind encouragements. This research was supported in part by AMED under Grant Number JP17gm0810011 (N.I.), JSPS KAKENHI (JP19H03223, N.I.), JSPS Grants-in-Aid for Early-Career Scientists (JP19K16127, K.B.), and the Osaka Medical Research Foundation for Incurable Diseases (K.B., T.M.).

AUTHOR CONTRIBUTION

K.Y., K.B., S.M., H.K.-K. and K.O. performed the experiments and data analyses. K.Y., K.B., T.M., S.M., H.K.-K., K.O., Y.H. and N.I. designed the experiments. K.Y., Y.S. and N.I. constructed the mathematical model. K.Y., T.M., Y.S., K.O. and N.I. wrote the manuscript. N.I. supervised all the projects. All authors discussed the results and commented on the manuscript.

DECLARATION OF INTERESTS

The authors declare that they have no competing financial interests.

INCLUSION AND DIVERSITY

We support inclusive, diverse, and equitable conduct of research.

REFERENCES

1. Pollard, T.D., and Borisy, G.G. (2003). Cellular motility driven by assembly and disassembly of actin filaments. Cell *112*, 453–465.
2. Bernstein, B.W., and Bamburg, J.R. (2010). ADF/cofilin: a functional node in cell biology. Trends Cell Biol. *20*, 187–195.
3. Carlier, M.F., and Shekhar, S. (2017). Global treadmilling coordinates actin turnover and controls the size of actin networks. Nat. Rev. Mol. Cell Biol. *18*, 389–401. 10.1038/nrm.2016.172.
4. Rottner, K., and Schaks, M. (2019). Assembling actin filaments for protrusion. Curr. Opin. Cell Biol. *56*, 53–63.
5. Gardel, M.L., Schneider, I.C., Aratyn-Schaus, Y., and Waterman, C.M. (2010). Mechanical integration of actin and adhesion dynamics in cell migration. Annu. Rev. Cell Dev. Biol. *26*, 315–333.
6. Mallavarapu, A., and Mitchison, T. (1999). Regulated actin cytoskeleton assembly at filopodium tips controls their extension and retraction. J. Cell Biol. *146*, 1097–1106.
7. Suter, D.M., and Forscher, P. (2000). Substrate-cytoskeletal coupling as a mechanism for the regulation of growth cone motility and guidance. J. Neurobiol. *44*, 97–113.
8. Tatavarty, V., Kim, E.J., Rodionov, V., and Yu, J. (2009). Investigating sub-spine actin dynamics in rat hippocampal neurons with super-resolution optical imaging. PLoS ONE *4*, e7724.
9. Loomis, P.A., Zheng, L., Sekerkova, G., Changyaleket, B., Mugnaini, E., and Bartles, J.R. (2003). Espin cross-links cause the elongation of microvillus-type parallel actin bundles in vivo. J. Cell Biol. *163*, 1045–1055.
10. Meenderink, L.M., Gaeta, I.M., Postema, M.M., Cencer, C.S., Chinowsky, C.R., Krystofiak, E.S., Millis, B.A., and Tyska, M.J. (2019). Actin dynamics drive microvillar motility and clustering during brush border assembly. Dev. Cell *50*, 545–556 e544.
11. Kovacs, E.M., Verma, S., Ali, R.G., Ratheesh, A., Hamilton, N.A., Akhmanova, A., and Yap, A.S. (2011). N-WASP regulates the epithelial junctional actin cytoskeleton through a non-canonical post-nucleation pathway. Nat. Cell Biol. *13*, 934–943.
12. Efimova, N., and Svitkina, T.M. (2018). Branched actin networks push against each other at adherens junctions to maintain cell-cell adhesion. J. Cell Biol. *217*, 1827–1845.

13. Rzadzinska, A.K., Schneider, M.E., Davies, C., Riordan, G.P., and Kachar, B. (2004). An actin molecular treadmill and myosins maintain stereocilia functional architecture and self-renewal. J. Cell Biol. *164*, 887–897.
14. Oser, M., Yamaguchi, H., Mader, C.C., Bravo-Cordero, J.J., Arias, M., Chen, X., Desmarais, V., van Rheenen, J., Koleske, A.J., and Condeelis, J. (2009). Cortactin regulates cofilin and N-WASp activities to control the stages of invadopodium assembly and maturation. J. Cell Biol. *186*, 571–587.
15. Albiges-Rizo, C., Destaing, O., Fourcade, B., Planus, E., and Block, M.R. (2009). Actin machinery and mechanosensitivity in invadopodia, podosomes and focal adhesions. J. Cell Sci. *122*, 3037–3049.
16. Gerisch, G. (2010). Self-organizing actin waves that simulate phagocytic cup structures. PMC Biophys. *3*, 7.
17. Goode, B.L., Eskin, J., and Shekhar, S. (2023). Mechanisms of actin disassembly and turnover. J. Cell Biol. *222*.
18. Vitriol, E.A., Wise, A.L., Berginski, M.E., Bamburg, J.R., and Zheng, J.Q. (2013). Instantaneous inactivation of cofilin reveals its function of F-actin disassembly in lamellipodia. Mol. Biol. Cell *24*, 2238–2247.
19. Carlsson, A.E. (2010). Actin dynamics: from nanoscale to microscale. Annu. Rev. Biophys. *39*, 91–110.
20. Allard, J., and Mogilner, A. (2013). Traveling waves in actin dynamics and cell motility. Curr. Opin. Cell Biol. *25*, 107–115.
21. Inagaki, N., and Katsuno, H. (2017). Actin waves: origin of cell polarization and migration? Trends Cell Biol. *27*, 515–526.
22. Beta, C., Edelstein-Keshet, L., Gov, N., and Yochelis, A. (2023). From actin waves to mechanism and back: How theory aids biological understanding. eLife *12*, e87181.
23. Weiner, O.D., Marganski, W.A., Wu, L.F., Altschuler, S.J., and Kirschner, M.W. (2007). An actin-based wave generator organizes cell motility. PLoS Biol. *5*, e221.
24. Katsuno, H., Toriyama, M., Hosokawa, Y., Mizuno, K., Ikeda, K., Sakumura, Y., and Inagaki, N. (2015). Actin migration driven by directional assembly and disassembly of membrane-anchored actin filaments. Cell Rep. *12*, 648–660.
25. Bechinger, C., Di Leonardo, R., Löwen, H., Reichhardt, C., Volpe, G., and Volpe, G. (2016). Active particles in complex and crowded environments. Rev. Mod. Phys. *88*, 045006.
26. Kaiser, A., Wensink, H.H., and Lowen, H. (2012). How to capture active particles.

Phys. Rev. Lett. *108*, 268307.

27. Elgeti, J., Winkler, R.G., and Gompper, G. (2015). Physics of microswimmers--single particle motion and collective behavior: a review. Rep. Prog. Phys. *78*, 056601.

28. Vutukuri, H.R., Hoore, M., Abaurrea-Velasco, C., van Buren, L., Dutto, A., Auth, T., Fedosov, D.A., Gompper, G., and Vermant, J. (2020). Active particles induce large shape deformations in giant lipid vesicles. Nature *586*, 52-56.

29. Vassilev, V., Platek, A., Hiver, S., Enomoto, H., and Takeichi, M. (2017). Catenins steer cell migration via stabilization of front-rear polarity. Dev. Cell *43*, 463-479.

30. Minegishi, T., Fujikawa, R., Kastian, R.F., Sakumura, Y., and Inagaki, N. (2021). Analyses of actin dynamics, clutch coupling and traction force for growth cone advance. J. Vis. Exp., e63227.

31. Kubo, Y., Baba, K., Toriyama, M., Minegishi, T., Sugiura, T., Kozawa, S., Ikeda, K., and Inagaki, N. (2015). Shootin1-cortactin interaction mediates signal-force transduction for axon outgrowth. J. Cell Biol. *210*, 663-676. 10.1083/jcb.201505011.

32. Flynn, K.C., Pak, C.W., Shaw, A.E., Bradke, F., and Bamburg, J.R. (2009). Growth cone-like waves transport actin and promote axonogenesis and neurite branching. Dev. Neurobiol. *69*, 761-779.

33. Minegishi, T., Uesugi, Y., Kaneko, N., Yoshida, W., Sawamoto, K., and Inagaki, N. (2018). Shootin1b mediates a mechanical clutch to produce force for neuronal migration. Cell Rep. *25*, 624-639.e626.

34. Nolen, B.J., Tomasevic, N., Russell, A., Pierce, D.W., Jia, Z., McCormick, C.D., Hartman, J., Sakowicz, R., and Pollard, T.D. (2009). Characterization of two classes of small molecule inhibitors of Arp2/3 complex. Nature *460*, 1031-1034.

35. Nishimura, Y., Shi, S., Zhang, F., Liu, R., Takagi, Y., Bershadsky, A.D., Viasnoff, V., and Sellers, J.R. (2021). The formin inhibitor SMIFH2 inhibits members of the myosin superfamily. J. Cell Sci. *134*, jcs253708.

36. Cameron, L.A., Robbins, J.R., Footer, M.J., and Theriot, J.A. (2004). Biophysical parameters influence actin-based movement, trajectory, and initiation in a cell-free system. Mol. Biol. Cell *15*, 2312-2323.

37. Kalwarczyk, T., Ziebacz, N., Bielejewska, A., Zaboklicka, E., Koynov, K., Szymanski, J., Wilk, A., Patkowski, A., Gapinski, J., Butt, H.J., and Holyst, R. (2011). Comparative analysis of viscosity of complex liquids and cytoplasm of mammalian cells at the nanoscale. Nano Lett. *11*, 2157-2163.

38. Bretschneider, T., Anderson, K., Ecke, M., Muller-Taubenberger, A., Schroth-Diez, B., Ishikawa-Ankerhold, H.C., and Gerisch, G. (2009). The three-dimensional dynamics of actin waves, a model of cytoskeletal self-organization. Biophys. J. *96*, 2888-2900.
39. Zhang, K., Lyu, W., Yu, J., and Koleske, A.J. (2018). Abl2 is recruited to ventral actin waves through cytoskeletal interactions to promote lamellipodium extension. Mol. Biol. Cell *29*, 2863-2873.
40. Ruthel, G., and Banker, G. (1998). Actin-dependent anterograde movement of growth-cone-like structures along growing hippocampal axons: a novel form of axonal transport? Cell Motil. Cytoskelet. *40*, 160-173.
41. Parker, K.K., Brock, A.L., Brangwynne, C., Mannix, R.J., Wang, N., Ostuni, E., Geisse, N.A., Adams, J.C., Whitesides, G.M., and Ingber, D.E. (2002). Directional control of lamellipodia extension by constraining cell shape and orienting cell tractional forces. FASEB J. *16*, 1195-1204.
42. Koestler, S.A., Auinger, S., Vinzenz, M., Rottner, K., and Small, J.V. (2008). Differentially oriented populations of actin filaments generated in lamellipodia collaborate in pushing and pausing at the cell front. Nat. Cell Biol. *10*, 306-313.
43. Gerisch, G., Bretschneider, T., Muller-Taubenberger, A., Simmeth, E., Ecke, M., Diez, S., and Anderson, K. (2004). Mobile actin clusters and traveling waves in cells recovering from actin depolymerization. Biophys. J. *87*, 3493-3503.
44. Hadjitheodorou, A., Bell, G.R.R., Ellett, F., Shastry, S., Irimia, D., Collins, S.R., and Theriot, J.A. (2021). Directional reorientation of migrating neutrophils is limited by suppression of receptor input signaling at the cell rear through myosin II activity. Nat. Commun. *12*, 6619.
45. De Belly, H., Yan, S., Borja da Rocha, H., Ichbiah, S., Town, J.P., Zager, P.J., Estrada, D.C., Meyer, K., Turlier, H., Bustamante, C., and Weiner, O.D. (2023). Cell protrusions and contractions generate long-range membrane tension propagation. Cell *186*, 3049-3061 e3015.
46. Tsujita, K., Takenawa, T., and Itoh, T. (2015). Feedback regulation between plasma membrane tension and membrane-bending proteins organizes cell polarity during leading edge formation. Nat. Cell Biol. *17*, 749-758.
47. Yamada, K.M., and Sixt, M. (2019). Mechanisms of 3D cell migration. Nat. Rev. Mol. Cell Biol. *20*, 738-752.
48. Jasnin, M., Ecke, M., Baumeister, W., and Gerisch, G. (2016). Actin organization in cells responding to a perforated surface, revealed by live imaging and cryo-electron tomography. Structure *24*, 1031-1043.

49. Hadjitheodorou, A., Bell, G.R.R., Ellett, F., Irimia, D., Tibshirani, R., Collins, S.R., and Theriot, J.A. (2023). Leading edge competition promotes context-dependent responses to receptor inputs to resolve directional dilemmas in neutrophil migration. Cell Syst. *14*, 196–209 e196.
50. Paoluzzi, M., Di Leonardo, R., Marchetti, M.C., and Angelani, L. (2016). Shape and displacement fluctuations in soft vesicles filled by active particles. Sci. Rep. *6*, 34146.
51. Li, Y., and Ten Wolde, P.R. (2019). Shape transformations of vesicles induced by swim pressure. Phys. Rev. Lett. *123*, 148003.
52. Boudet, J.F., Lintuvuori, J., Lacouture, C., Barois, T., Deblais, A., Xie, K., Cassagnere, S., Tregon, B., Bruckner, D.B., Baret, J.C., and Kellay, H. (2021). From collections of independent, mindless robots to flexible, mobile, and directional superstructures. Sci. Robot. *6*, eabd0272.
53. Huber, L., Suzuki, R., Kruger, T., Frey, E., and Bausch, A.R. (2018). Emergence of coexisting ordered states in active matter systems. Science *361*, 255–258.
54. Okano, K., Matsui, A., Maezawa, Y., Hee, P.Y., Matsubara, M., Yamamoto, H., Hosokawa, Y., Tsubokawa, H., Li, Y.K., Kao, F.J., and Masuhara, H. (2013). In situ laser micropatterning of proteins for dynamically arranging living cells. Lab Chip *13*, 4078–4086.
55. Baba, K., Yoshida, W., Toriyama, M., Shimada, T., Manning, C.F., Saito, M., Kohno, K., Trimmer, J.S., Watanabe, R., and Inagaki, N. (2018). Gradient-reading and mechano-effector machinery for netrin-1-induced axon guidance. eLife *7*, e34593.
56. Toriyama, M., Shimada, T., Kim, K.B., Mitsuba, M., Nomura, E., Katsuta, K., Sakumura, Y., Roepstorff, P., and Inagaki, N. (2006). Shootin1: A protein involved in the organization of an asymmetric signal for neuronal polarization. J. Cell Biol. *175*, 147–157.
57. Higashiguchi, Y., Katsuta, K., Minegishi, T., Yonemura, S., Urasaki, A., and Inagaki, N. (2016). Identification of a shootin1 isoform expressed in peripheral tissues. Cell Tissue Res. *366*, 75–87.

FIGURE LEGENDS

Figure 1. Actin waves emerge widely in cells

(A) A fluorescence image of a U251 cell expressing EGFP-LifeAct obtained by TIRF microscopy. Asterisk indicates cellular leading edge. See Video S1. Scale bar, 20 µm.

(B) Fluorescence time-lapse images of filopodium-type (arrowheads) and lamellipodium-type (arrows) actin waves in U251 cells expressing LifeAct-mCherry obtained by TIRF microscopy. Filopodium-type waves frequently changed their direction of translocation (yellow arrowheads): some emerged and separated (yellow and cyan arrowheads) from lamellipodium-type waves (arrows) or branched off from filopodium-type waves (green arrowheads See Video S1. Scale bar, 2 µm.

(C and D) Fluorescence time-lapse images of actin waves on the dorsal membrane (blue arrowheads and arrows, C) and filopodium-type actin waves in cytoplasm (green arrowheads, D) in U251 cells expressing LifeAct-mCherry obtained by 3D imaging with confocal deconvolution microscopy. See Video S2. Scale bars, 1 µm.

(E and F) Fluorescence time-lapse images of a U251 cell expressing LifeAct-mCherry (obtained by TIRF microscopy) and EGFP-LifeAct (obtained by epifluorescence microscopy): right panel and (F) indicate enlarged time-lapse images in rectangular regions 1 and 2. See Video S2. Scale bars, 5 µm (E); 1 µm (E enlarged view, F). See also Figure S1.

Figure 2. Actin waves translocate by treadmilling

(A) A fluorescent speckle image of HaloTag-actin in a U251 cell obtained by TIRF microscopy; actin filaments were also monitored by EGFP-LifeAct. Time-lapse montages of a filopodium-type actin wave in the rectangular region at 10-sec intervals are shown to the right. Green and magenta lines indicate wave forward translocation and actin filament retrograde flow, respectively. Actin polymerization rate can be calculated as the sum of the forward translocation rate and actin retrograde flow rate (double-headed arrow). See Video S3. Scale bars, 5 µm (left); 1 µm (right).

(B) A diagram showing the translocation mechanisms of actin waves travelling on the ventral plasma membrane (left)[24]. Right panel shows a possible mode of actin wave translocation observed in Figures 1C and 1D. For explanations, see text.

(C) A fluorescence image of a U251 cell stained with anti-shootin1b antibody and Alexa

Fluor 594 conjugated phalloidin (for actin filament) obtained by TIRF microscopy. An enlarged view of the area within the rectangle is shown in the right panel. Arrowheads indicate shootin1b colocalization with actin filaments. Scale bars, 20 µm (left); 5 µm (right).

(D) Translocation velocities of filopodium-type actin waves (green line, A) before and after the application of DMSO (control, N = 4 cells: before application, n = 34 waves; after application, n = 32 waves), CK666 (N = 3 cells: before application, n = 49 waves; after application, n = 33 waves) or SMIFH2 (N = 5 cells: before application, n = 52 waves; after application, n = 37 waves). Data represent means ± SEM; ***$p < 0.01$; *$p < 0.05$; ns, not significant. Statistical analyses were performed using the two-tailed Mann–Whitney *U*-test.

(E) Velocities of actin filament retrograde flow (magenta line, A), actin filament polymerization (double-headed arrow, A), and translocation (green line, A) of filopodium-type waves in WT and shootin1b KO U251 cells (WT, N = 11 cells, n = 71 waves; KO#1, N = 9 cells, n = 69 waves; KO#2, N = 10 cells, n = 45 waves). Data represent means ± SEM; ***$p < 0.01$; *$p < 0.05$; ns, not significant. Statistical analyses were performed using the two-tailed Mann–Whitney *U*-test. See also Figure S1.

Figure 3. Actin waves as precursors of protrusions

(A and B) Fluorescence time-lapse images of filopodium-type (A) and lamellipodium-type (B) actin waves arrived at the cell periphery in U251 cells expressing EGFP-LifeAct obtained by epifluorescence microscopy (A) and expressing LifeAct-mCherry obtained by TIRF microscopy (B). They pushed the plasma membrane, resulting in the formation of filopodia (arrowheads) and lamellipodium (yellow arrows), and continued to move laterally along the membrane. The latter merged with the pre-existing lamellipodium (blue arrows). See Videos S4 and S5. Scale bars, 5 µm.

(C) Fluorescence time-lapse images of a filopodium-type actin wave (arrowheads) which entered into a pre-existing lamellipodium (arrows) in U251 cells expressing EGFP-LifeAct obtained by TIRF microscopy. Entry of the wave into lamellipodia resulted in local actin filament accumulation and lamellipodial extension (arrows). See Video S6. Scale bar, 1 µm.

(D) A diagram describing the relationship between the velocities of lateral movement

(V_L) and ventral movement (V_V) of filopodium-type actin waves. If actin waves move laterally along the membrane driven by directional actin treadmilling, V_L is equal to $V_V \cos\theta$, where θ is the angle of the polymerizing actin filaments with respect to the membrane.

(E) Fluorescence time-lapse images of a filopodium-type actin wave travelling along the lateral membrane (arrowheads) of a U251 cell expressing LifeAct-mCherry obtained by epifluorescence microscopy. See Video S7. The right graph shows V_L and θ obtained by the time-lapse imaging; V_L closely matched $V_V\cos\theta$ (N = 10 cells, n = 21 waves). Scale bar, 5 µm.

Figure 4. Actin filaments and a component of Arp2/3 complex accumulate at protrusions

(A and B) Fluorescence time-lapse images of filopodium-type (arrowheads, A) and lamellipodium-type (arrows, B) actin waves which accumulated in protrusive regions (asterisks) in U251 cells expressing EGFP-LifeAct obtained by epifluorescence microscopy. See Video S8. Scale bars, 20 µm (B); 5 µm (A).

(C) Preparation of a laminin-coated adhesive island. A triangular pattern of adhesive laminin substrate with the edge length 35 µm and the area 530.4 μm^2 was created. The cell-adhesive patterns generated were confirmed by coating with green fluorescent-HiLyte 488-Laminin (for details see STAR METHODS).

(D) A U251 cell cultured on a laminin-coated triangular adhesive island and stained with Alexa Fluor 594 conjugated phalloidin (for actin filament), anti-ARPC2 antibody, and DAPI (for nucleus). Scale bar, 20 µm.

(E) Fluorescence time-lapse images of a U251 cell expressing LifeAct-mCherry cultured on a triangular adhesive island. The images were obtained by epifluorescence microscopy. Arrowheads indicate an actin wave travelled along the lateral membrane, resulting in a local accumulation of actin filaments at the corner upon arrival. See Video S9. Scale bar, 20 µm.

Figure 5. Actin waves mediate actin filament accumulation at the cell periphery and protrusions

(A and B) Mathematical model data showing actin wave localization in a triangular cell (A) and cells with different corner angles, 30º, 60º, 120º or 180º (B), presented in arbitrary unit (a.u.). See Video S10. The right graph in (B) shows quantitative data for the actin wave accumulation at the corners with different corner angles (30-180º, n = 20 model data). Data represent means ± SEM; ***p < 0.01. Statistical analyses were performed using the two-tailed unpaired Student′s *t*-test (180º vs 120º, 120º vs 60º) and two-tailed unpaired Welch′s *t*-test (60º vs 30º).

(C) U251 cells cultured on laminin-coated adhesive islands with the different corner angles and stained with Alexa Fluor 594 conjugated phalloidin and DAPI. The right graph shows quantitative data for the actin filament accumulation at the corners (30º, N = 6 experiments, n = 22 cells; 60º, N = 8 experiments, n = 23 cells; 120º, N = 7 experiments, n = 26 cells; 180º, N = 8 experiments, n = 18 cells). Scale bar, 20 µm. Data represent means ± SEM; ***p < 0.01; ns, not significant. Statistical analyses were performed using the two-tailed unpaired Student′s *t*-test (180º vs 120º) and two-tailed Mann–Whitney *U*-test (120º vs 60º, 60º vs 30º).

(D) Mathematical model data showing actin wave localization in a triangular shootin1b KO cell. See Video S10. The right graphs show quantitative data for actin wave accumulation at the edge and corners of WT and shoootin1b KO cells (WT, KO, n = 20 model data). Data represent means ± SEM; ***p < 0.01. Statistical analyses were performed using the two-tailed unpaired Student′s *t*-test.

(E) A shootin1b KO#1 U251 cell cultured on a laminin-coated triangular adhesive island and stained with Alexa Fluor 594 conjugated phalloidin and DAPI. The right graphs show quantitative data for actin filament accumulation at the edge and corners of WT and shoootin1b KO cells (WT, N = 3 experiments, n = 13 cells; KO#1, N = 6 experiments, n = 11 cells). Scale bar, 20 µm. Data represent means ± SEM; **p < 0.02; *p < 0.05. Statistical analyses were performed using the two-tailed unpaired Welch′s *t*-test (left) and two-tailed unpaired Student′s *t*-test (right). See also Figure S2.

Figure 6. Actin waves drive spontaneous formation of the leading edge for cell migration

(A) WT, shootin1b KO#1 and KO#2 U251 cells stained with Alexa Fluor 594 conjugated phalloidin and DAPI. Scale bar, 50 µm.

(B and C) Lamellipodial coverage rate (B) and histogram of lamellipodia localization at cell periphery (C) of WT, shootin1b KO#1 and KO#2 U251 cells in (A) (WT, KO#1, KO#2, N = 3 experiments, n = 35 cells). Scale bar, 5 μm. Data represent means ± SEM; ***$p < 0.01$; *$p < 0.05$; ns, not significant. Statistical analyses were performed using the two-tailed unpaired Student′s *t*-test (B; KO#1 vs KO#2) and two-tailed unpaired Welch′s t-test (B; WT vs KO#1, WT vs KO#2).

(D) Fluorescence time-lapse images of a WT U251 cell expressing LifeAct-mCherry obtained by epifluorescence microscopy: lower panels indicate enlarged time-lapse images of the areas indicated by the dashed yellow boxes 1 and 2. The images were taken before and after the treatment with 100 nM latrunculin A (Lat A), and at the indicated times after the Lat A washout. The asterisks indicate actin filament-enriched nascent lamellipodia. Yellow and blue arrows indicate enlargement and lateral expansions of nascent lamellipodia, respectively. See Video S11. Scale bars, 20 μm; 5 μm (enlarged views).

(E and F) Mathematical model data showing actin wave localization in WT and shootin1b KO cells bearing nascent lamellipodia (E) and integrated filopodium (F), presented in arbitrary unit (a.u.). The panels below describe the cell shape (40 μm width). The graphs below show quantitative data for actin wave accumulation at the nascent lamellipodia (E) and integrated filopodium (F) of WT and shoootin1b KO cells (WT, KO, n = 20 model data). Data represent means ± SEM; ***$p < 0.01$. Statistical analyses were performed using the two-tailed unpaired Student′s *t*-test.

(G) Fluorescence time-lapse images of a shootin1b KO#1 U251 cell expressing LifeAct-mCherry obtained by epifluorescence microscopy. The images were taken before and after the treatment with 100 nM Lat A, and at the indicated times after the Lat A washout. The asterisks indicate nascent lamellipodia. See Video S11. Scale bar, 20 μm. See also Figure S3.

Figure 7. A model of cell morphogenesis driven by treadmilling actin waves

(A) A model of the translocation mechanisms of treadmilling actin waves. During the translocation, the front and rear ends of waves move forward via polymerization and disassembly, respectively (blue arrows). Shootin1b facilitates the wave translocation by impeding their retrograde flow (Figure 2B left). As the local concentrations of actin

subunits and actin-binding proteins decrease at the front by polymerization and increase at the rear by disassembly, they diffuse along the local concentration gradients (red and green arrows). Accompanied by the directional diffusion, actin waves mediate the translocation of actin and actin-binding proteins.

(B) Actin wave arrival at the cell periphery aligns randomly oriented actin filaments towards outward polymerization, which in turn pushes the membrane to protrude (gray arrows). Shootin1b also facilitates this protrusion step by mechanically coupling the treadmilling actin filaments and the adhesive substrate[33].

(C) Actin waves self-accumulate at cell protrusions (yellow arrows), leading to their further growth (gray arrows).

(D) Self-accumulation of actin waves at protrusions (green arrow) constitutes a positive feedback interaction with actin-mediated cell protrusion (red box), thereby conferring robustness to the classical pathway of cellular morphogenesis (black arrows). Actin waves are regulated under cell signaling (Black and blue arrows). This system can also respond to extracellular topographic cues that deform the plasma membrane from outside (yellow arrow).

(E) Processes of spontaneous polarization of glioma cells. Through local protrusion (B) and lateral expansion (C), nascent lamellipodia are formed and integrated into a large leading edge for polarization.

STAR METHODS

KEY RESOURCES TABLE

REAGENT or RESOURCE	SOURCE	IDENTIFIER
Antibodies		
Rabbit polyclonal anti-shootin1	(Toriyama et al., 2006)	N/A
Rabbit polyclonal anti-shootin1b	(Higashiguchi et al., 2016)	N/A
Goat polyclonal anti-NCAM-L1	Santa Cruz Biotechnology	Cat# sc-1508; RRID: AB_631086
Mouse monoclonal anti-cortactin	Millipore	Cat# 05-180; RRID: AB_309647
Mouse monoclonal anti-actin	Millipore	Cat# MAB1501R; RRID: AB_2223041
Rabbit polyclonal anti-ARPC2	Millipore	Cat# 07-227
Alexa 594 conjugated donkey anti-rabbit	Jackson ImmunoResearch Labs	Cat# 711-585-152; RRID: AB_2340621
Alexa 488 conjugated goat anti-rabbit	Thermo Fisher Scientific	Cat# A-11008; RRID: AB_143165
Alexa 488 conjugated goat anti-mouse	Thermo Fisher Scientific	Cat# A-11029; RRID: AB_2534088
HRP conjugated donkey anti-rabbit	Cytiva	Cat# NA934; RRID: AB_772206

HRP conjugated goat anti-mouse	Thermo Fisher Scientific	Cat# AP308P; RRID: AB_92635
Chemicals, Peptides, and Recombinant Proteins		
Alexa 594 phalloidin	Thermo Fisher Scientific	Cat# A12381
DAPI	Thermo Fisher Scientific	Cat# D1306
Poly-D-lysine	Sigma	Cat# P6407-5MG
Laminin	Wako	Cat# 120-05751
HaloTag TMR ligand (5mM)	Promega	Cat# G8251
LIPIDURE (MPC-polymer)	NOF	Cat# CM5206
3-phenylaminopropyltrimethoxysilane	Shin-Etsu	Cat# LS-4500
Cell lines		
U251	A gift from Drs. Masatoshi Takeichi (Riken) and Shintaro Suzuki (Kwabsei Gakuin Univ)	(Vassilev et al., 2017)
U-251 Shootin1b-KO	This paper	N/A
COS7	Riken BRC	Cat# RCB0539
Oligonucleotides		
Shootin1b-Exon1 F 5´-CACCGGCAGCTCATTACCAGTCTGA-3´	This paper	N/A
Shootin1b-Exon1 R 5´-AAACTCAGACTGGTAATGAGCTGCC-3´	This paper	N/A
LifeAct F	This paper	N/A

5´-TCGAGATGGGTGTCGCAGATTTGATCAAGAAATTCGAAAGCATCTCAAAGGAAGAAGGG-3´		
LifeAct R 5´-GATCCCTTCTTCCTTTGAGATGCTTTCGAATTTCTTGATCAAATCTGCGACACCCATC-3´	This paper	N/A
Recombinant DNA		
pFN21A-HaloTag-actin	(Minegishi et al., 2018)	N/A
pEGFP-N1-LifeAct	This paper	N/A
pmcherry-N1-LifeAct	This paper	N/A
pSpCas9(BB)-2A-Puro (PX459) V2.0	Addgene	Cat# 62988
Software and Algorithms		
ImageJ software	National Institutes of Health	https://imagej.nih.gov/ij/index.html; RRID: SCR_003070
GraphPad Prism7	GraphPad Software	https://www.graphpad.com/; RRID: SCR_002798
MATLAB Version R2021a	Mathworks	https://www.mathworks.com/products/new_products/release2021a.html; RRID: SCR_001622
ZEN software	Carl Zeiss	https://www.zeiss.com/microscopy/i

		nt/products/microscope-software/zen.html; RRID: SCR_013672
Metamorph	Molecular Devices	https://www.moleculardevices.com/products/cellular-imaging-systems/acquisition-and-analysis-software/metamorph-microscopy; RRID:SCR_002368
Las X	Leica	https://www.leica-microsystems.com/products/microscope-software/p/leica-las-x-ls/; RRID:SCR_013673
Deposited Data		
Source data of immunoblot and statistical analyses in the Figures	This paper	DOI: 10.17632/ymmcbh92v6.1
The MATLAB codes used for mathematical modeling	This paper	https://github.com/KioYagami/actin-wave/tree/master

RESOURCE AVAILABILITY

Lead Contact

Further information and requests for resources and reagents should be directed to and will be fulfilled by the Lead Contact, Naoyuki Inagaki (ninagaki@bs.naist.jp).

Materials Availability

All unique materials generated in this study are available from the Lead Contact without restriction.

Data and Code Availability

- Source data of immunoblot and statistical analyses in the Figures have been deposited at Mendeley Data (DOI: 10.17632/ymmcbh92v6.1) and are publicly available as of the date of publication.
- The MATLAB codes used for mathematical modeling are available at GitHub (https://github.com/KioYagami/actin-wave/tree/master).
- Any additional information required to reanalyze the data reported in this paper is available from the lead contact upon request.

EXPERIMENTAL MODEL AND SUBJECT DETAILS

Cell culture and transfection

A subline of glioma U251 cells[29] and COS7 cells were seeded on glass-bottom dishes (Matsunami, #D11130H) coated with 100 μg/ml poly-D-lysine (Sigma) and 5 μg/ml laminin (Lonza), and cultured in DMEM high glucose medium (Nacalai, #08458-16) supplemented with 10% fetal bovine serum (Japan Bio Serum) at 37°C and 5% CO_2. They were transfected with vectors using Polyethylenimine MAX (PEI MAX, Polysciences) following the manufacturer's protocol.

Generation of shootin1b KO U251 cells by CRISPR-Cas9

The guide oligonucleotide sequence (forward: 5´-CACCGGCAGCTCATTACCAGTCTGA-3´; reverse: 5´-AAACTCAGACTGGTAATGAGCTGCC-3´), corresponding to nucleotides 30-49 in the

coding region of human shootin1b, were selected by an online CRISPR Cas9 Design tool (http://crispr.mit.edu/). The pSpCas9(BB)-2A-Puro (PX459) V2.0 plasmid (Addgene, #62988) was linearized using by BbsI-HF (New England Biolabs, #R3539S), then the guide oligonucleotides were annealed and inserted into the vector using Ligation high Ver.2 (TOYOBO, #LGK-201). U251 cells were transfected with the plasmid, cultured individually in 96-well plates, and screened using 4 μg/ml puromycin. Shootin1b depletion in KO cells was confirmed by immunoblot analyses (Figure S1I).

METHOD DETAILS

Micropatterning of laminin on the substrate for cell adhesion

Micropatterns of laminin for cell adhesion were produced on a glass surface following our previously established procedure[54], with modifications (Figure 4C). The glass-bottom dish (Iwaki, #3961-035) was cleaned using ultrasonic waves for 5 min with special grade ethanol, followed by rinsing with water and additional 5-min ultrasonic cleaning with pure water. After the cleaning, the dish was air-dried in a clean room at room temperature. 3-Phenylaminopropyltrimethoxysilane (2%, Shin-Etsu, #LS-4500) was dissolved in a 2% solution of acetic acid in water and then poured onto the glass-bottom dish, followed by incubation for 30 min. After being washed twice with water, the dish was dried at 70°C for 1 h. This process resulted in the covalent bonding of the 3-phenylaminopropyl group with the glass surface, which made it hydrophobic. Any residues resulting from the reaction were eliminated by ultrasonically cleaning with special grade ethanol for 5 min.

The hydrophobic glass surface was coated with 100 μL of ethanol containing 0.2% of MPC (2-methacryloyloxyethyl phosphorylcholine) polymer (NOF, #Lipiduro-CM5206). After the reaction for 10-15 sec, the coating solution was removed and left to dry overnight at room temperature in the dark. This resulted in the formation of an MPC polymer film on the glass. Then, the dish was incubated with 2 ml H_2O overnight. In the film, the phosphatidylcholine residues of the MPC polymers are oriented towards the aqueous solution (Figure 4C).

The cell non-adhesive MPC-polymer layer was removed by a programmed raster scanning of a femtosecond laser (center wavelength 800 nm, pulse width 130 fsec, pulse energy 100 nJ, transmission frequency 5 kHz, Solstice, Spectra-Physics) focused with an objective lens 20x 0.46 NA (Olympus, UMPlanFl) at a speed of 400 μm/s on the glass

surface. The raster scanning patterns are shown Figures 4C and S2F. Then, the cell-adhesive patterns of laminin were produced by coating the exposed glass surface with poly-D-lysine (PDL) and laminin. The cell-adhesive patterns were confirmed by coating with green fluorescent-HiLyte 488-Laminin (Cytoskeleton, #LMN02-A) (Figure 4C).

Immunocytochemistry

Immunocytochemistry was performed as described previously[55]. Cultured cells were fixed with 3.7% formaldehyde in Krebs buffer (118 mM NaCl, 4.7 mM KCl, 1.2 mM KH_2PO_4, 1.2 mM $MgSO_4$, 4.2 mM $NaHCO_3$, 2 mM $CaCl_2$, 10 mM glucose, 400 mM sucrose, 10 mM HEPES pH 7.0) for 20 min on ice and 10 min at room temperature, followed by treatment for 15 min with 0.05% Triton X-100 in PBS on ice and 10% fetal bovine serum in PBS for 1 h at room temperature. The cells were incubated with a primary antibody diluted in PBS containing 10% fetal bovine serum overnight at 4°C. They were washed with PBS, and then incubated with secondary antibody diluted in PBS for 1 h at room temperature. After washing with PBS, the cells were stained with Alexa Fluor 594 conjugated phalloidin (1:100, Thermo Fisher Scientific) and DAPI (1:1000, Thermo Fisher Scientific) for 30 min at room temperature. The fluorescence and phase-contrast images of U251 cells were acquired a fluorescence microscope (Carl Zeiss, Axioplan2) equipped with an objective lens 40x 0.75 NA (Carl Zeiss, plan-Neofluar), a charge-coupled device camera (Carl Zeiss, AxioCam MRm) and imaging software (Carl Zeiss, ZEN), and a TIRF microscope (Olympus, IX81) equipped with a CMOS camera (Hamamatsu, ORCA Flash4.0LT), an objective lens 100x 1.49 NA (Olympus, UAPON), and MetaMorph software.

Immunoblot

Cultured U251 cells were lysed with RIPA buffer (50 mM Tris-HCl (pH 8.0), 1 mM EDTA, 150 mM NaCl, 1% Triton X-100, 0.1% SDS, 0.1% sodium deoxycholate, 1 mM DTT, 1 mM PMSF, and 0.01 mM leupeptin), and incubated for 10 min at 4°C. Subsequently, the cell lysate was centrifuged at 15000 rpm for 15 min at 4°C. The supernatant was mixed with an equal volume of 2 x SDS sample buffer (131 mM Tris-HCl, pH 6.8, 21% glycerol, 4% SDS, 0.05% bromophenol blue and 5% β-mercaptoethanol). The mixture was incubated for 5 min at 95°C, followed by SDS-

polyacrylamide gel electrophoresis. Immunoblotting was performed as described previously[33].

Antibodies

The following primary antibodies were used: anti-shootin1 (rabbit, 1:400) [56]; anti-shootin1b (rabbit, 1:2000) [57]; anti-NCAM-L1 (mouse, 1:1000, Santa Cruz Biotechnology, #sc-514360); anti-cortactin (mouse, 1:1000, Millipore, #05-180); anti-actin (mouse, 1:1000, Millipore, #MAB1501R); anti-ARPC2 (rabbit, 1:1000, Millipore, #07-227). The following secondary antibodies were used: anti-rabbit (Alexa 594 conjugated donkey, 1:1000, Jackson ImmunoResearch Labs, #711-585-152); anti-rabbit (Alexa 488 conjugated goat, 1:1000, Thermo Fisher Scientific, #A-11008); anti-mouse (Alexa 488 conjugated goat, 1:1000, Thermo Fisher Scientific, #A-11029); anti-rabbit (HRP conjugated donkey, 1:2000, GE Healthcare, #NA934); anti-mouse (HRP conjugated goat, 1:5000, Thermo Fisher Scientific, #AP308P).

DNA construction

To generate pEGFP-N1-LifeAct vector, the annealed LifeAct (forward: 5´-TCGAGATGGGTGTCGCAGATTTGATCAAGAAATTCGAAAGCATCTCAAAGGAAGAAGGG-3´; reverse: 5´-GATCCCTTCTTCCTTTGAGATGCTTTCGAATTTCTTGATCAAATCTGCGACACCCATC-3´) was fused to N-terminal of EGFP-N1 vectors (Clontech). To generate pLifeAct-mCherry-N1 vector, the annealed LifeAct was fused to N-terminal of mCherry-N1 vectors (Takara, #632523). Generation of pFN21A-HaloTag-actin was described previously[33].

TIRF and epifluorescence microscopy

U251 cells were cultured on glass-bottom dishes coated with PDL and laminin. Actin dynamics in close proximity to the ventral plasma membrane were visualized using the actin filament marker EGFP-LifeAct or LifeAct-mCherry under TIRF or epifluorescence microscopy. In addition, to differentially visualize actin waves translocating in close proximity to the ventral plasma membrane and those detached from the membrane, we combined TIRF microscopy, which visualizes the region in close proximity to the ventral

plasma membrane, and epifluorescence microscopy, which visualizes the entire cell thickness (Figure 1E). U251 cells expressing LifeAct-mCherry and EGFP-LifeAct were cultured on glass-bottom dishes coated with PDL and laminin. Prior to observation, the cells were incubated in DMEM/F-12 Ham medium (Sigma) supplemented with 10% FBS (Japan Bio Serum). The TIRF laser was used to observe fluorescence images of LifeAct-mCherry, while the epifluorescence laser was used to observe fluorescence images of EGFP-LifeAct. The observations were made with a TIRF microscope (Olympus, IX81) equipped with a CMOS camera (Hamamatsu, ORCA Flash4.0LT), an objective lens 100x 1.49 NA or 150x 1.45 NA (Olympus, UAPON), and MetaMorph software. Images were acquired every 10 or 60 sec.

Fluorescent speckle imaging of actin wave by TERF microscopy

Actin dynamics within waves were examined the by labelling actin filaments with EGFP-LifeAct, and monitoring actin molecules in waves by speckle imaging of HaloTag-actin[30]. U251 cells expressing HaloTag-actin and EGFP-LifeAct were cultured on glass-bottom dishes coated with PDL and laminin. Prior to observation, the cells were treated with 0.05 μM HaloTag TMR ligand (Promega) in the culture medium and incubated for 1 h at 37°C. The ligand was washed with PBS, and the cells were then incubated in DMEM/F-12 Ham medium (Sigma, #D8062) supplemented with 10% FBS (Japan Bio Serum). The fluorescent speckles of HaloTag-actin and EGFP-LifeAct were observed using a TIRF microscope (Olympus, IX81) equipped with a CMOS camera (Hamamatsu, ORCA Flash4.0LT), an objective lens 150x 1.45 NA (Olympus, UAPON), and MetaMorph software. Fluorescence images were acquired every 10 sec. Actin flow velocity was calculated by tracing the speckles of HaloTag-actin in actin waves using ImageJ (Fiji version). Actin polymerization rate was calculated as the sum of actin wave migration velocity, visualized by EGFP-LifeAct, and HaloTag-actin flow velocity, as reported[30].

3D imaging by confocal deconvolution microscopy

U251 cells expressing HaloTag-actin and EGFP-LifeAct were cultured in 2D (on glass-bottom dishes coated with PDL and laminin) or 3D (75% matrigel) environment. Before observation, the cells were incubated with 0.05 μM HaloTag TMR ligand (Promega) in the culture medium and incubated for 1 h at 37°C. The ligand was washed with PBS, and

the cells were then incubated in DMEM/F-12 Ham medium (Sigma) supplemented with 10% FBS (Japan Bio Serum). The fluorescent speckles of HaloTag-actin and EGFP-LifeAct were observed using a confocal microscope (Leica, Stellaris 8) equipped with an objective lens 100x 1.40 NA (Leica, HC PL APO CS2) and Las X software. Deconvolution of 3D image stacks were obtained by Las X software.

Mathematical modelling

To investigate whether actin waves mediate the accumulation of actin filaments at the protrusions of cells confined to adhesive islands (Figure 4D), we constructed a mathematical model that describes the movement of intracellular actin waves. Our model is based on quantitative data obtained from experimental observations: we focused on filopodium-type waves because it is difficult to observe individual actin filaments in lamellipodium-type waves, and filopodium-type and lamellipodium-type waves are interchangeable (Figure 1B). For simplicity, the present model describes the translocation of the actin filament arrays, not a detailed mechanism of wave translocation[24]. The model depicts the processes of wave emergence and disappearance, as well as changes in the direction of wave translocation.

Emergence and disappearance of actin waves

Our experimental data indicate that actin waves emerge widely in the cytoplasm, move in random directions, and then disappear (Video S1). In our model, the emergence locations and translocation directions of actin waves are randomly chosen at the start of the modeling. The model data are updated every 1 sec ($\Delta t = 1$ sec), generating one actin wave in the cell with a probability of 10%. The lifetimes of actin waves in WT and shootin1b KO cells, quantified by live cell imaging, were modeled using gamma distributions (Figures S2A and S2B).

The length (L) and translocation velocity (V) of actin waves are also derived from experimental data (Figures 2E and S2E); model uses their average values for simplicity. Actin waves located at the cell periphery move laterally along the cell membrane (Figure 3A). The velocity of the lateral movement was modelled as $\cos\theta$ of the mean velocity of actin waves (Figure 2E), where θ is the angle of the direction of wave movement with respect to the cell membrane (Figure 3E).

The local concentration of actin subunits increases immediately after the disappearance (complete disassembly) of actin wave (Figure 3C). Since actin polymerization depends on the local concentration of actin subunits, our model assumes that an actin wave reemerges at the location where the preceding wave disappeared and translocates in a random direction.

Change in the direction of wave translocation

Actin waves frequently change the direction of their translocation (Videos S1). The change in direction was quantified every 50 sec from live cell imaging data (Figure S2D). As the angular distribution of these changes was symmetric with a zero peak, we modelled it using a Gaussian distribution (Figure S2D).

Model parameters estimated from experimental data

- Translocation velocity of actin wave (Figure 2E): 2.0 μm/min (WT), 1.5 μm/min (KO#1)
- Actin wave length (Figure S2E): 4.1 μm
- Parameters of the gamma distribution representing lifetime variation; estimated from quantitative data (Figures S2A and S2B): α = 3.0, β = 119 (WT), α = 2.4, β = 106 (KO#1)
- Parameters of the Gaussian distribution representing actin wave directional change; quantified from experimental data (Figure S2D): μ = -0.61, σ = 11

Analyses of actin filament accumulation and lamellipodial formation

Accumulation of actin filaments at the cell periphery was determined by dividing the average fluorescence intensity of actin filaments within a 2 μm-wide region from the cell periphery (green region, Figure S2G) by the average intensity of actin filaments in the whole cell region (blue region). Accumulation of actin filaments at the cell protrusions was determined by dividing the average intensity of actin filaments at the corner regions (yellow region: 2 μm-wide and 5 μm-long regions in both sides of the corner, Figure S2G) by the average intensity of actin filaments in the peripheral region (green region). Accumulation of actin filaments at the nascent lamellipodia was determined by dividing

the average fluorescence intensity of actin filaments in protrusive regions (green regions, Figure S3C) by the average intensity of actin filaments in the whole cell region (blue region). Accumulation of actin filaments at the integrated lamellipodium was determined by dividing the average intensity of actin filaments at the convex leading edge (yellow region: 4 μm-wide, Figure S3D) by the average intensity of actin filaments in the rear region (green region: 4 μm-wide). Lamellipodial coverage rate was calculated by dividing the total length of lamellipodia (yellow line, Figure S3A) by the perimeter of the cell (green line). The fluorescence intensity of actin filaments was analyzed using ImageJ (Fiji version). Lamellipodia was defined as the area of cell periphery where the fluorescence intensity exceeded the mean intensity + SD of the whole cell body. The polar histogram of the lamellipodial areas was generated using MATLAB (Figure 6C).

Quantification and statistical analyses

Statistical analyses were performed using Excel (Microsoft 365) or GraphPad Prism 7 (GraphPad Software). For samples with more than 7 data points, the D′Agostino–Pearson normality test was used to determine whether the data followed a normal distribution. In cases where the number of data points was between 3 and 7, the Shapiro–Wilk test was used for the normality test. We also tested the equality of variation with the F test for two independent groups that followed normal distributions. Significance tests were performed as follows: (1) two-tailed unpaired Student′s *t*-test to compare normally distributed data with equal variance from two independent groups; (2) two-tailed unpaired Welch′s *t*-test to compare normally distributed data with unequal variance from two independent groups; (3) two-tailed Mann–Whitney *U*-test to compare nonnormally distributed data from two independent groups. The statistical information and number of samples for each experiment are indicated in the Figure legends. For detailed statistical results including the test statistics and exact p values, see the statistical source data associated with each Figure. All data are shown as the mean ± SEM. Statistical significance was defined as ***$p < 0.01$; **$p < 0.02$; *$p < 0.05$; ns, not significant. All experiments were performed at least three times and reliably reproduced. The investigators were blinded to the experimental groups for each analysis.

SUPPLEMENTAL VIDEO LEGENDS

Video S1. Related to Figures 1 and S1

First part: U251 cells expressing EGFP-LifeAct observed by TIRF microscopy. Left: filopodium-type and lamellipodium-type actin waves emerged widely in the cytoplasm, moved in random directions, and disappeared (see Figure 1A). Right: filopodium-type waves changed the direction of their translocation randomly (yellow arrowheads); some emerged and separated (yellow and cyan arrowheads) from lamellipodium-type waves (arrow) or branched off (cyan arrowheads) from filopodium-type waves (see Figure 1B). Some lamellipodium-type waves expanded from the filopodium-type waves (arrows). Time interval: 10 sec. Scale bar: 20 µm (left), 10 µm (right).

Second part: actin waves moving on the ventral plasma membrane of a COS7 cell expressing LifeAct-mCherry observed by TIRF microscopy (see Figure S1D). Time interval: 60 sec. Scale bar: 20 µm.

Video S2. Related to Figure 1

First part: an actin wave translocating through the cytoplasm without interacting with the plasma membrane (see Figure 1D). A U251 cell expressing LifeAct-mCherry was observed by 3D imaging with confocal deconvolution microscopy. Time interval: 13 sec. Z-stack interval: 0.2 µm. Scale bar: 5 µm.

Second part: a U251 cell expressing LifeAct-mCherry observed by TIRF microscopy and EGFP-LifeAct observed by epifluorescence microscopy (see Figures 1E and 1F). Actin waves observed by epifluorescence microscopy and TIRF microscopy are indicated by green and magenta arrowheads, respectively. Time interval: 60 sec.

Video S3. Related to Figure 2

Fluorescent speckle dynamics of HaloTag-actin in a filopodium-type wave; actin filaments were also monitored by EGFP-LifeAct. They were observed by TIRF microscopy. The actin wave underwent treadmilling and translocated in the direction of polymerization (see Figure 2A). A Time interval: 10 sec. Scale bar: 1 µm.

Video S4. Related to Figure 3

Filopodia formation by filopodium-type actin waves (arrowheads) (see Figure 3A). A U251 cell expressing EGFP-LifeAct was observed by epifluorescence microscopy. Time interval: 10 sec. Scale bar: 5 µm.

Video S5. Related to Figure 3

Lamellipodium formation by a lamellipodium-type actin wave (yellow arrow) (see Figure 3B). A U251 cell expressing LifeAct-mCherry was observed by TIRF microscopy. The lamellipodium-type wave merged with the pre-existing lamellipodia (cyan arrow) through lateral movement. Time interval: 60 sec. Scale bar: 5 µm.

Video S6. Related to Figure 3

Filopodium-type actin waves entering into pre-existing lamellipodium (left) and filopodium (asterisk, right). The wave entry resulted in local actin filament accumulation and lamellipodial expansion (arrow) (See Figure 3C). U251 cells expressing EGFP-LifeAct were observed by TIRF microscopy. Time interval: 10 sec. Scale bars: 1 µm.

Video S7. Related to Figure 3

Filopodium-type actin waves travelling along the lateral membranes (see Figure 3E). U251 cells expressing LifeAct-mCherry were observed by epifluorescence microscopy. Time interval: 10 sec. Scale bars: 5 µm.

Video S8. Related to Figure 4

Filopodium-type actin waves (arrowheads) and a lamellipodium-type actin wave (arrow) accumulating at protrusive regions (asterisks) (see Figures 4A and 4B). U251 cells expressing EGFP-LifeAct were observed by epifluorescence microscopy. Time interval: 10 sec. Scale bars: 5 µm (left), 20 µm (right).

Video S9. Related to Figure 4

Actin wave accumulation at the corners of a triangular U251 cell (see Figure 4E). A U251 cell expressing LifeAct-mCherry was cultured on a triangular adhesive island and observed by epifluorescence microscopy. Actin waves travelled along the lateral edge,

resulting in local accumulation of actin filaments at the corners upon arrival (arrowheads). Time interval: 300 sec. Scale bar: 10 µm.

Video S10. Related to Figure 5

Mathematical model data showing actin wave accumulation in WT and shootin1b KO triangular cells (see Figures 5A and 5D). Time interval: 10 sec. Scale bars: 5 µm.

Video S11. Related to Figure 6

Fluorescence time-lapse Videos of WT and shootin1b KO#1 U251 cells expressing LifeAct-mCherry and observed by epifluorescence microscopy (see Figures 6D and 6G). The images were taken before and after the treatment with 100 nM latrunculin A, and after the Lat A washout. Time interval: 60 sec. Scale bars: 20 µm.

Figure 1 Yagami et al.

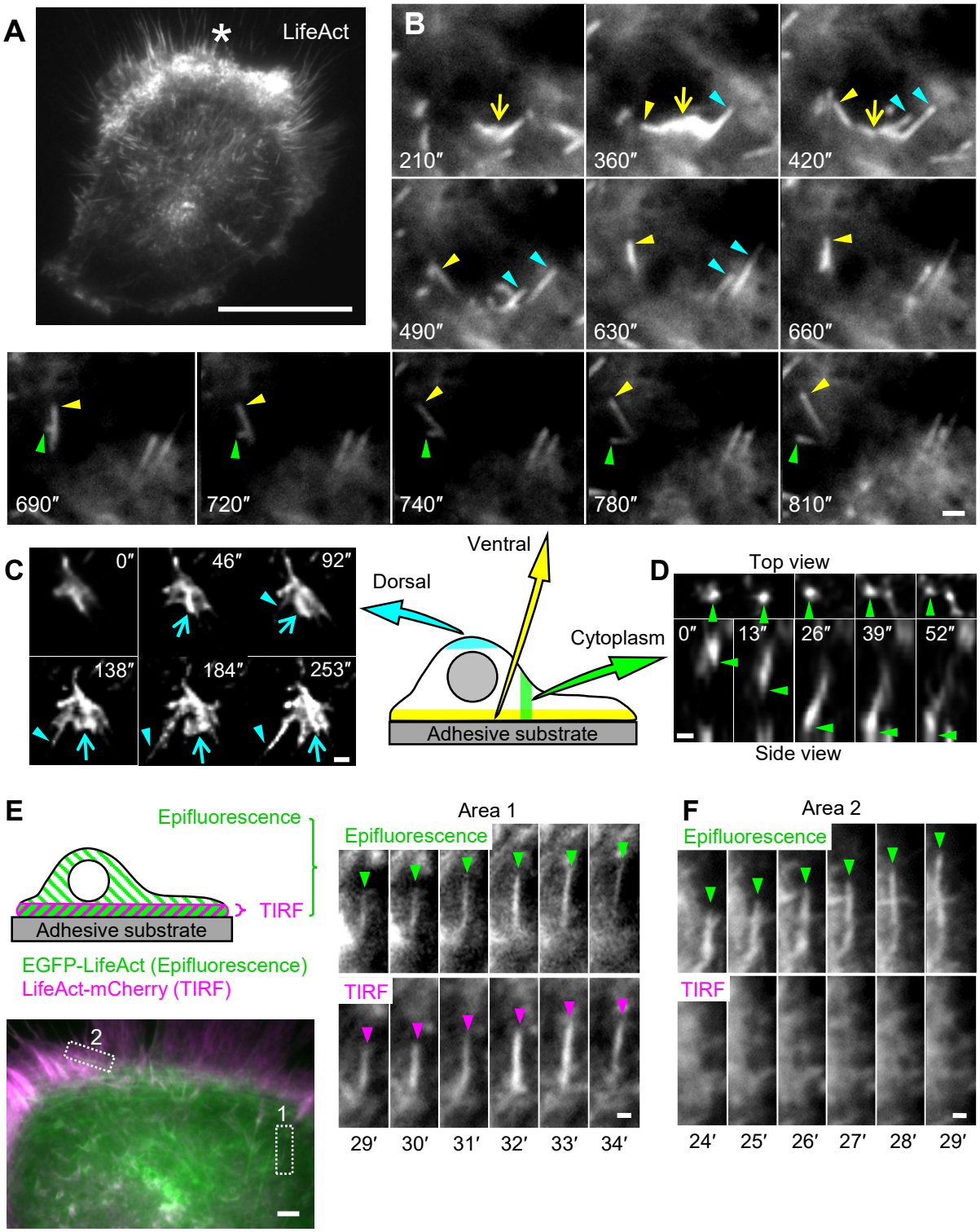

Figure 2 Yagami et al.

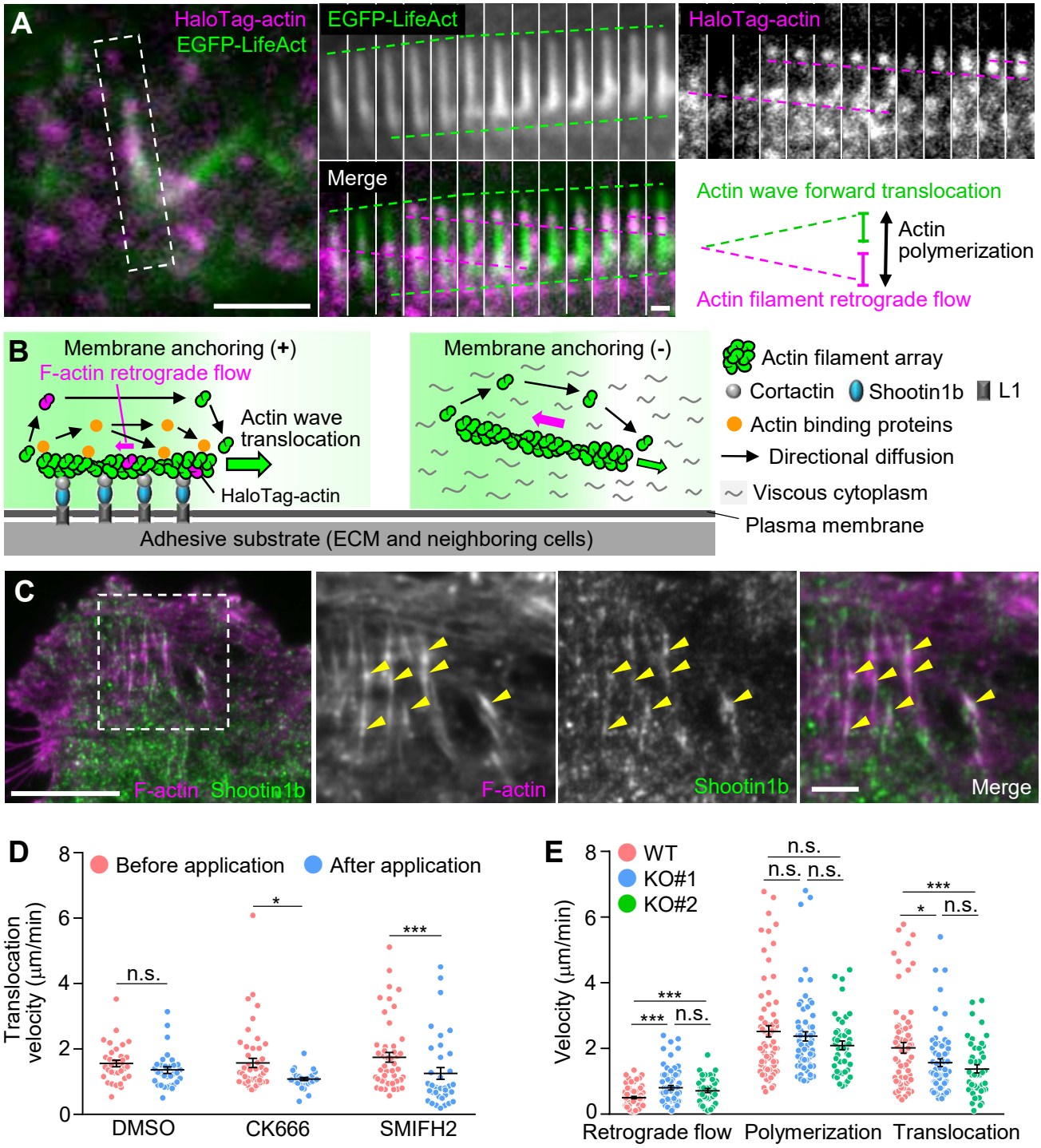

Figure 3 Yagami et al.

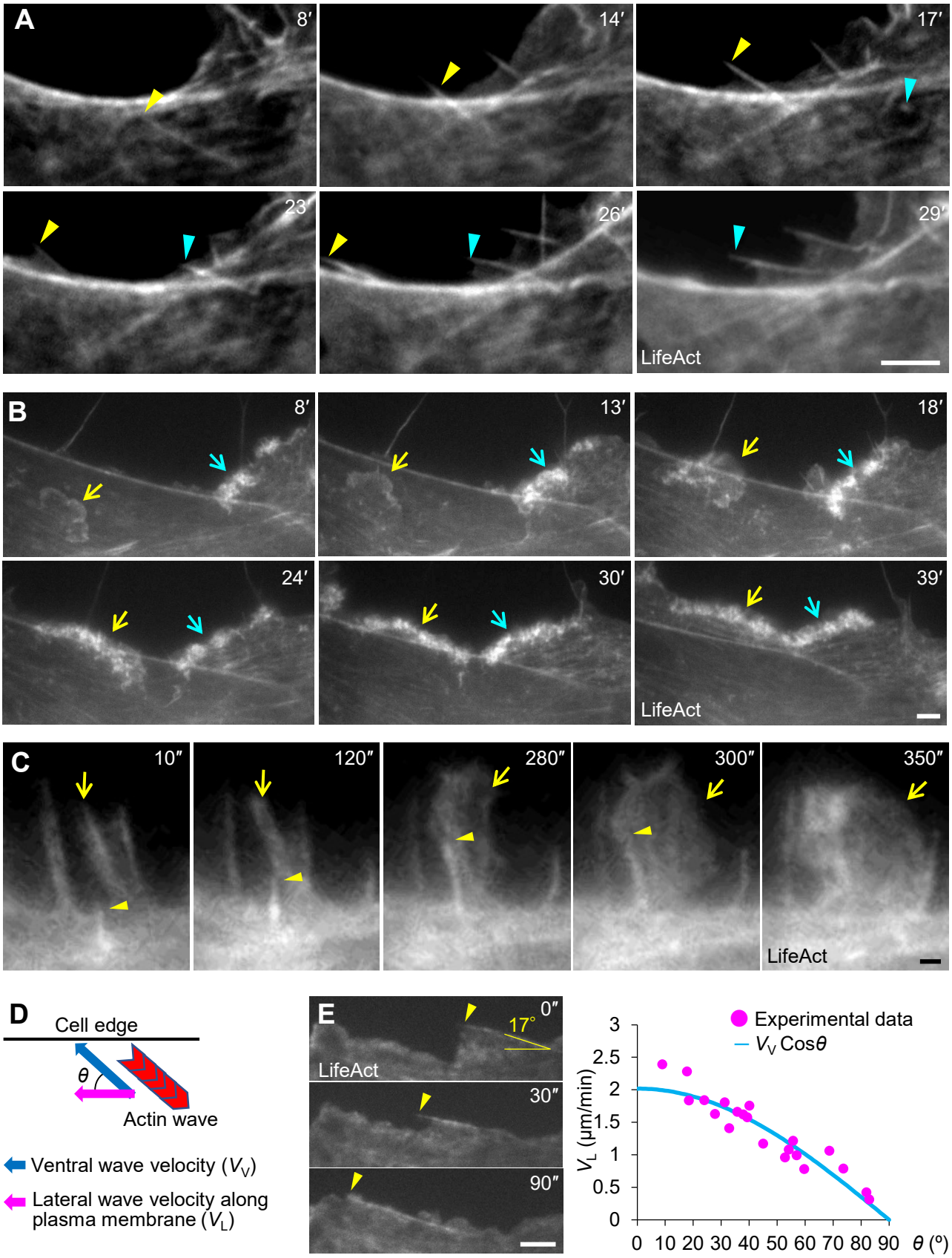

Figure 4 Yagami et al.

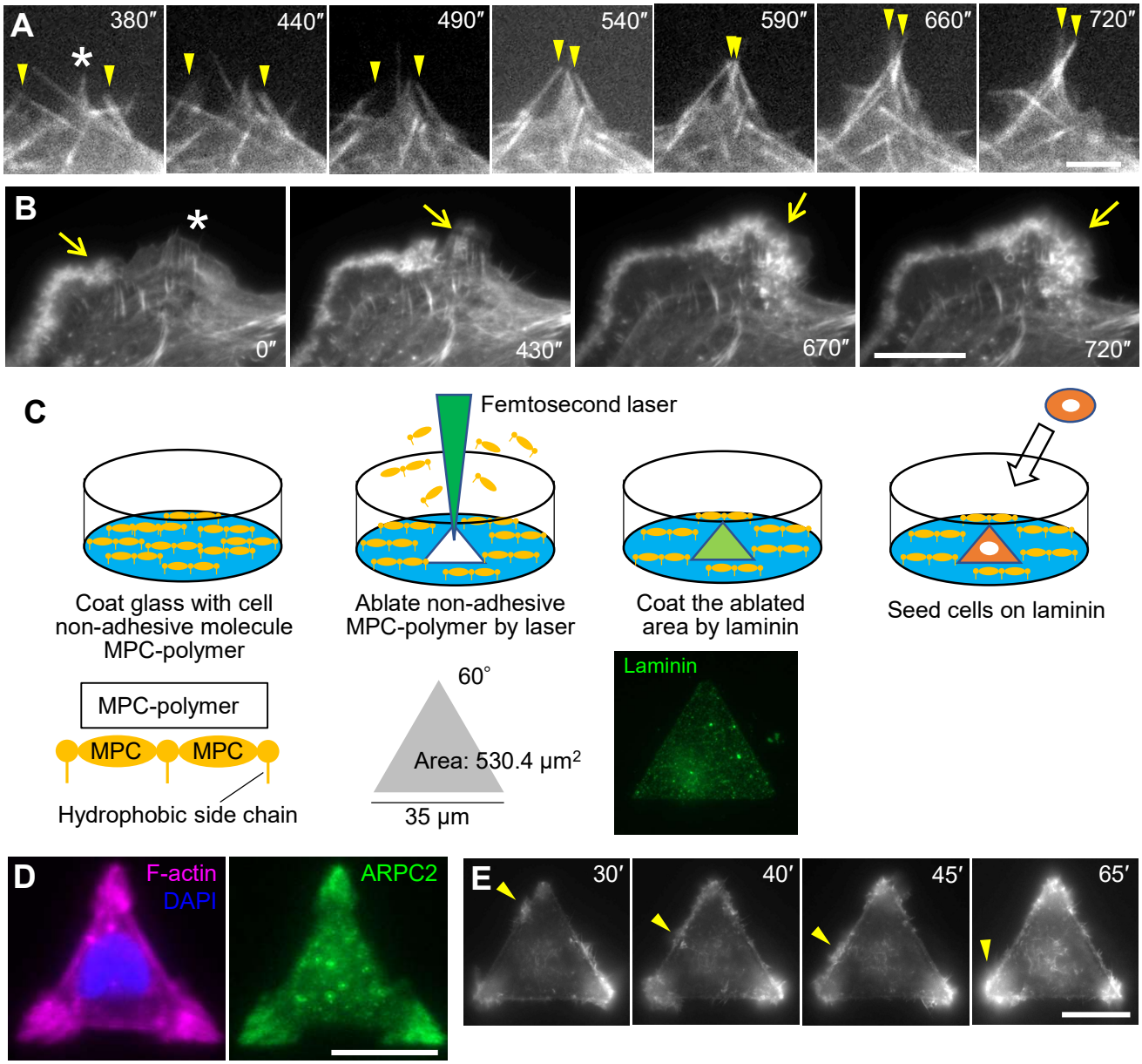

Figure 5 Yagami et al.

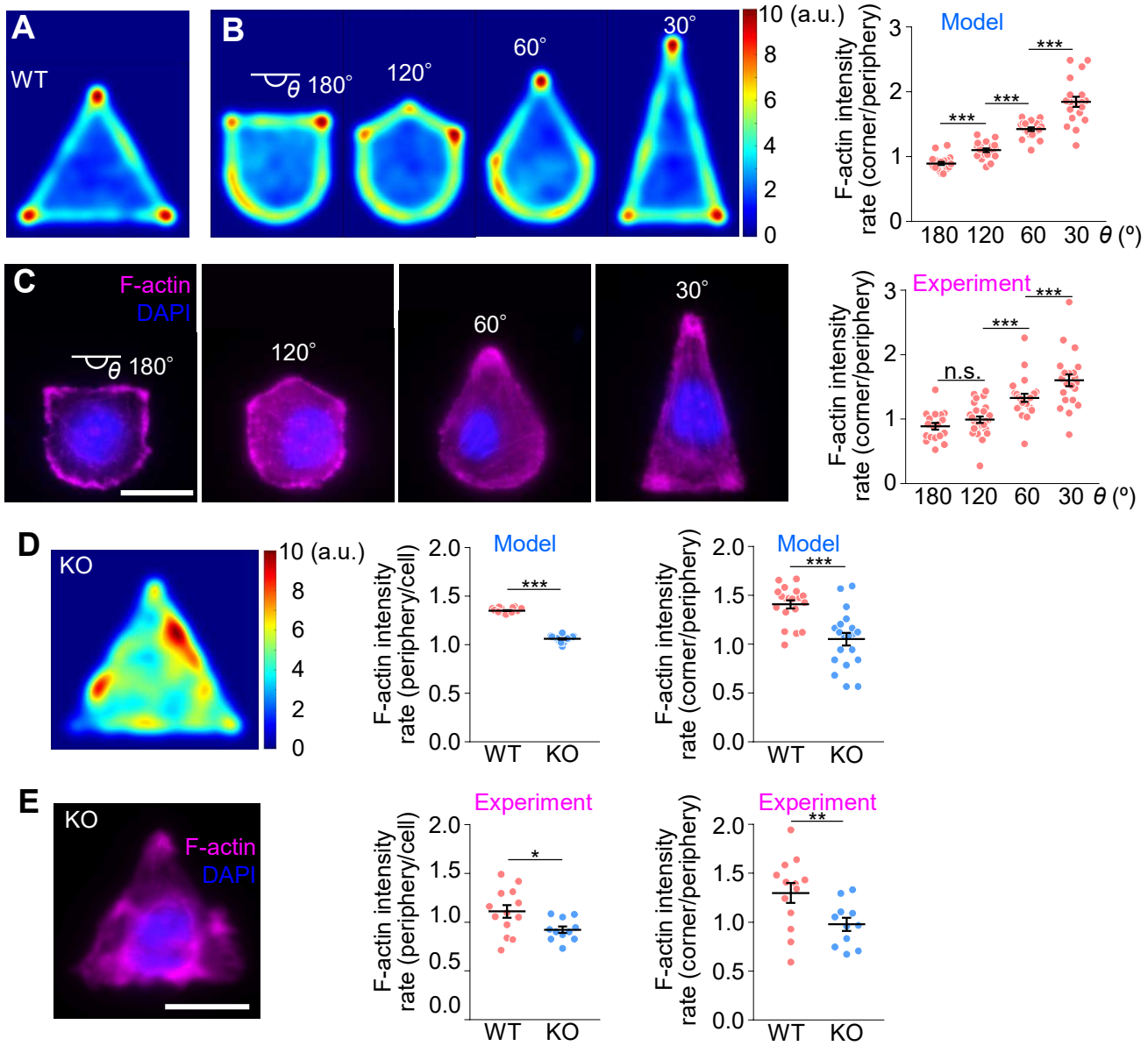

Fig. 6 Yagami et al.

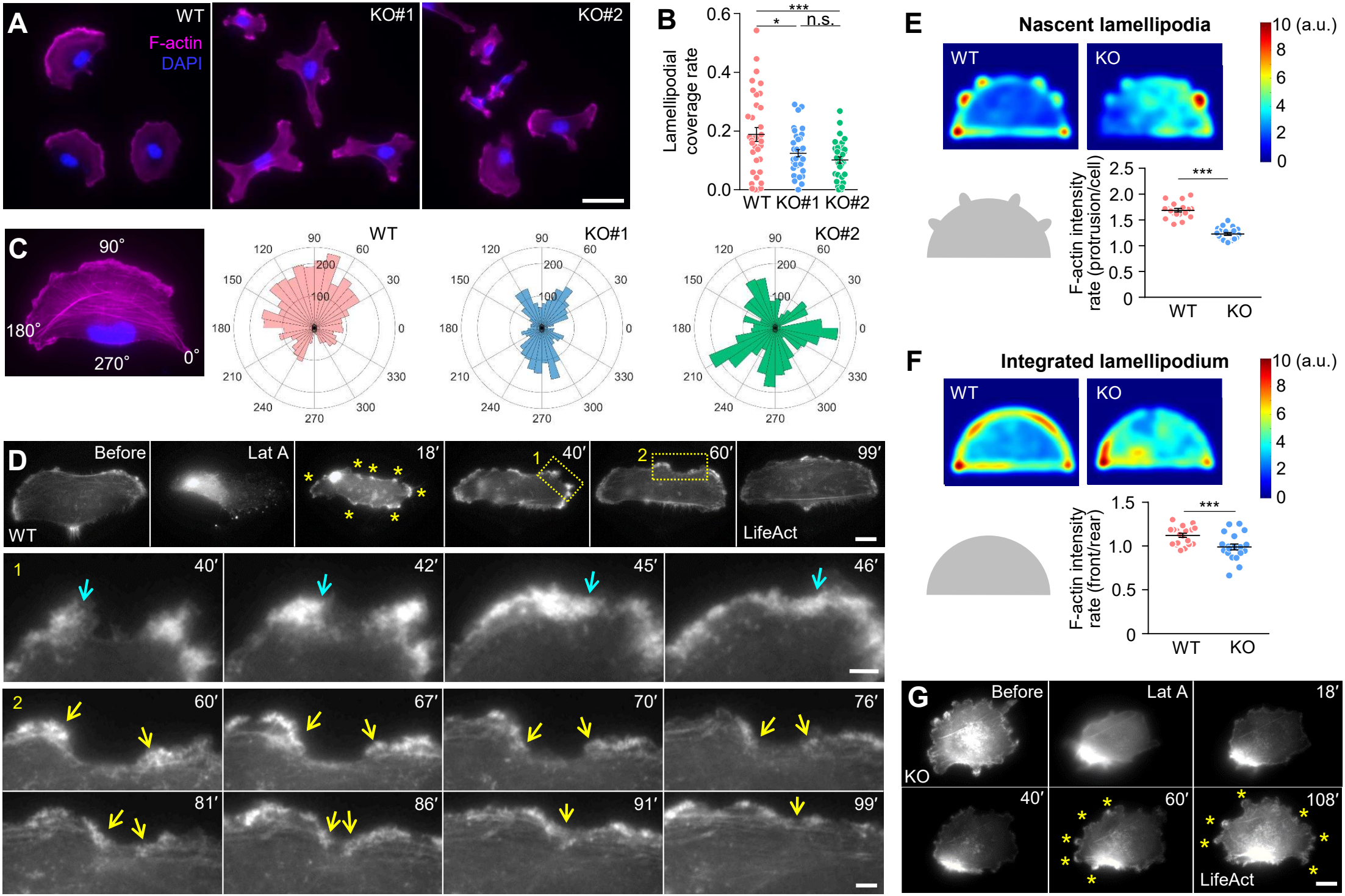
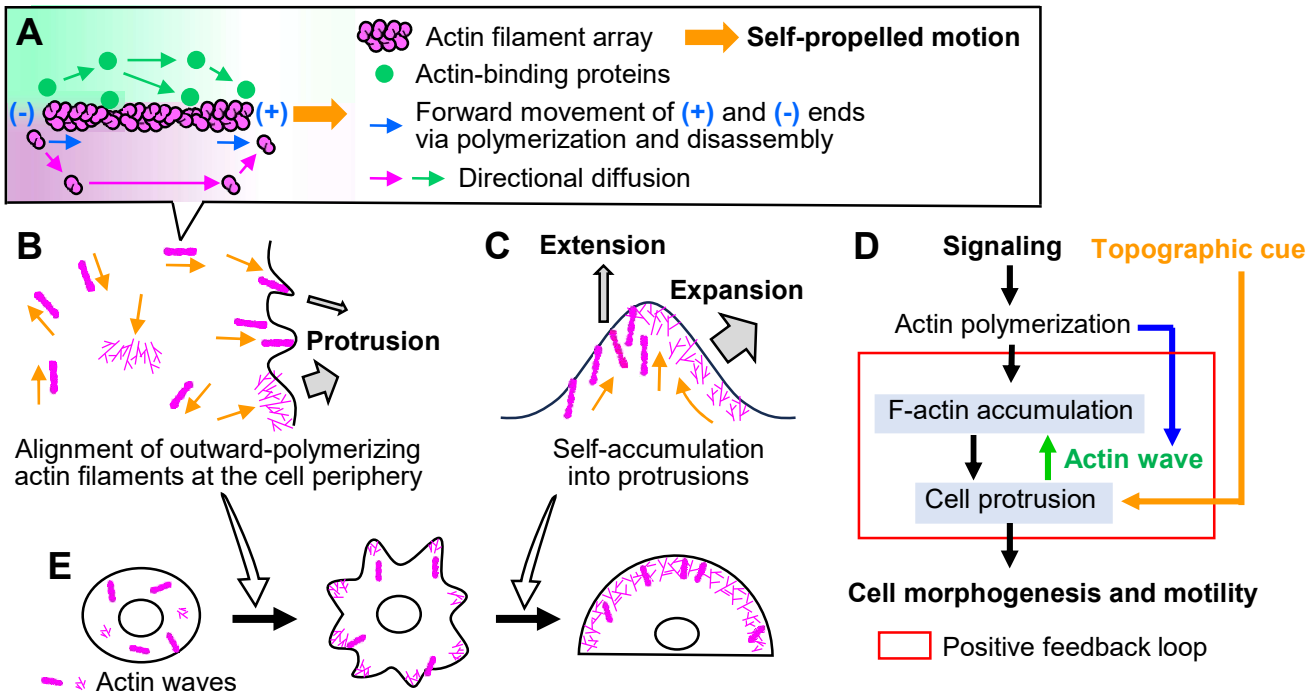
Figure 7 Yagami et al.